JOURNAL OF PROPULSION AND POWER
Vol. 14, No. 3, May–June 1998

Load Oscillations Caused by Unstart of Hypersonic Wind Tunnels and Engines

Takashi Shimura,* Tohru Mitani,† Noboru Sakuranaka,‡ and Muneo Izumikawa§
National Aerospace Laboratory, Miyagi 981-15, Japan

Large-amplitude load oscillations were observed during the tests of a hypersonic engine model in a freejet-type wind tunnel. To clarify the cause of the oscillations and their characteristics, oscillating wall pressures and loads on a drag model and engine models were investigated. Flowfield was observed by shadowgraph to determine the cause of the large starting loads. Power spectral density functions and probability functions of wall pressures and loads were derived by the fast Fourier transform. The amplitude of the unsteady frontal pressure was correlated with the dynamic pressure. The magnitude of the starting load was related to the drag coefficient of the models, and the expected maximum peak loads of a large-scale ramjet engine test facility were evaluated. Engine unstart loads were also simulated by means of secondary flow injection into a small-scale model of a ramjet engine. With these methods, characteristics of engine unstart loads and the possibility of sensing engine unstart in its early phase were studied. Engine unstart could be sensed with pressure measurement around the engine throat before it became severe. Furthermore, engine unstart loads associated with scramjet engine combustion were related to the drag coefficient of the engine.

Nomenclature

A_f = frontal area of test piece
C_d = drag coefficient, $F_d/A_f/q$
C_{dp} = peak load coefficient, $F_u/A_f/q$
F_d = drag without fuel injection
F_p = pressure drag, $A_f \times P_{20}$
F_u = peak value of unsteady loads caused by unstart of engines or wind tunnels
M = Mach number
$P(x)$ = cumulative probability distribution function, time interval with $X_{AC} \leq x$ in total sampling time, Prob$\{X_{AC} \leq x\}$
P_0 = nozzle total pressure
P_{20} = frontal pressure, pitot pressure
q = dynamic pressure of freejet
$\bar{X}$ = mean value of $X(t)$
X_{AC} = $X(t) - \bar{X}$
$X(t)$ = time-dependent sample functions
σ = standard deviation of X_{AC}

Introduction

DURING wind-tunnel start, a fluctuating load, defined as the starting load that is several times larger than steady load, is usually imposed on the force measurement system (FMS).[1,2] To prevent damage caused by the starting load, methods such as locking the FMS until wind-tunnel start, injecting a model into a wind tunnel after start, etc.,[1] are often used. However, starting load is still a serious problem, particularly in engine wind tunnels designed to simulate combustion. For example, injection of a model was abandoned in the design of the Ramjet Engine Test Facility (RJTF) of the National Aerospace Laboratory in Japan[3] to prevent problems arising from plumbing of liquid hydrogen and gaseous hydrogen. Moreover, because model size is large in the case of engine wind tunnels, the starting load encountered is possibly much greater than that of aerodynamic wind tunnels. If FMSs are sufficiently strong to withstand the severe starting loads, it is difficult to obtain sufficient accuracy for resolving the much smaller loads during tests. Therefore, it is necessary to predict starting load exactly and to investigate the mechanism of generation of a large starting load for safe and accurate test operations.

The unstart condition of engines also introduces large-amplitude load oscillations[4,5] in addition to the starting loads of wind tunnels. If the cause of large oscillations is starting loads of the wind tunnel, it is possible to prevent overloading of the FMS by the aforementioned means such as a lock system, etc. In case of engine unstart, however, it is impossible to protect the FMS from overloading quickly enough with these methods. Therefore, it is desirable to investigate characteristics of engine unstart loads and to sense incipient engine unstart. Engine unstart behavior is closely related to conditions of ramjet and scramjet engine inlets, and unsteady pressure behavior in an unfueled ramjet/scramjet inlet has been reported.[6]

In the present study, engine unstart loads were investigated by measuring and analyzing instantaneous loads and pressures using a one-fourth-scale model of the CH4-fueled subscale ramjet engine for the hypersonic civil transport (HYPR) (Ref. 7) cruising at Mach 5. Engine unstart conditions were controlled by injecting secondary flow into the one-fourth scale model.

Scramjet engine combustion tests at Mach 4, 6, and 8 flight conditions[8–11] were also conducted in the RJTF. Starting loads of the RJTF and engine unstart loads were measured under FMS unlocked conditions. Before the unlocked tests, loads under unlocked conditions were estimated by dynamic and static force transmission coefficient tests of the FMS lock system, and safe operation under unlocked condition tests was confirmed in advance. Hydrogen fuel flow rate was varied to investigate whether or not the scramjet engine shows large amplitude load and pressure oscillations caused by engine unstart as with the ramjet engine. Load and pressure oscillations

Presented as Paper 96-3242 at the AIAA/ASME/SAE/ASEE 32nd Joint Propulsion Conference, Lake Buena Vista, FL, July 1–3, 1996; received Feb. 27, 1997; revision received Oct. 29, 1997; accepted for publication Oct. 29, 1997.

*Head, Ramjet Control Systems Section, Kakuda Research Center, Kimigaya, Kakuda. Member AIAA.
†Head, Ramjet Combustion Section, Kakuda Research Center, Kimigaya, Kakuda. Member AIAA.
‡Senior Researcher, Ramjet Control Systems Section, Kakuda Research Center, Kimigaya, Kakuda.
§Senior Researcher, Ramjet Combustion Section, Kakuda Research Center, Kimigaya, Kakuda.

caused by engine unstart will be discussed in the latter half of this report.

Test of a Drag Model

Test Facility and Drag Model

Figure 1 shows the blowdown-type small-scale wind tunnel used in small-scale model tests. Its scale is one-fifth that of the RJTF. Three types of nozzles, M3.4, M4.1, and M5.3, were used for the tunnel. The nozzles were attached to a test cell that was a 570 mm × 300 mm × 300 mm rectangular parallelepiped. Wind tunnels of this type in which the cross-sectional area of a test cell is larger than the exit area of a nozzle are called freejet-type wind tunnels and are often used for engine tests. Room-temperature air was used as the working fluid.

A drag model was made to investigate starting loads. Figure 2 shows the drag model. The cross section of the model was a 26 mm × 26 mm square, and the length was 300 mm. Six flush-mount-type pressure sensors were installed on the front, back, upper, lower, left, and right surfaces of the model to measure the pressure variation during the process of wind-tunnel start. The natural frequency of the pressure sensors was 20 kHz.

In aerodynamic studies, it is customary to use an FMS installed in a sting holding a model. However, in the case of an engine wind tunnel, an FMS holding a model by means of a strut, rigidly installed on the wall of the tunnel, as shown in Fig. 1, is usually used. For the present study, an FMS using a roller table supported by linear roller bearings and able to slide only in the direction of flow was developed.

Process of Wind-Tunnel Start

Figure 3 shows variations of the front (pitot) pressure and the drag of the model. The front pressure corresponded to the pitot pressure at the exit of the wind-tunnel nozzle. The wind tunnel started at 30 s where the nozzle total pressure was 3.0 MPa. After reaching the maximum pressure, it decreased gradually until the minimum running pressure was 2.2 MPa.

The flush-mounted pressure sensor installed on the front face of the model showed atmospheric pressure from the start of blowdown to the point where region ① began. During this period, axial load measured by a load cell was small. In the region between 11 and 22 s, fluctuations of the model pitot pressure and drag increased more rapidly than the increase in nozzle total pressure.

When the nozzle total pressure reached 2.2 MPa, at 22 s, fluctuation amplitude, and mean values of the pressure and drag suddenly became small. The region between this point and wind-tunnel start is designated region ②.

Front pressure and drag were proportional to nozzle total pressure in region ③. Namely, after wind-tunnel start, front pressure showed a pitot pressure corresponding to the design Mach number, and drag showed the value expected from $P_{20} \times A_f$. The design Mach number flow broke at 48 s and the front pressure fluctuation amplitude in region ④ was almost the same as that in region ②.

Results of the high-response measurement shown in Fig. 3 indicate that the model encountered an extremely high pitot pressure of almost 1 MPa, which was about three times greater than the steady value after the wind-tunnel start. Therefore, we attempted to interpret the cause of high pitot pressure from the viewpoint of the flowfield.

Flowfield Just Before Wind-Tunnel Start

Figure 4 illustrates the flowfield of regions ① and ② in Fig. 3. To consider the mechanism of generation of the high pitot pressure, the flowfield around the nozzle just before the wind-tunnel start was observed with the shadowgraph method. The shadowgraph of region ① showed that waves alternately appeared at the upper or lower front of the drag model, which indicated that the flowfield was supersonic locally. The shadowgraph of region ② showed a jet boundary running from the edge of the nozzle exit, but did not show the wave structure observed during the wind-tunnel start.

The pressure history (envelope) in Fig. 3 may mislead readers by suggesting that the front of the model was always subjected to high pressure of almost 1 MPa in region ①. However, careful examination shows that such a high pressure was impulsive and that the duration of measurement of the high pres-

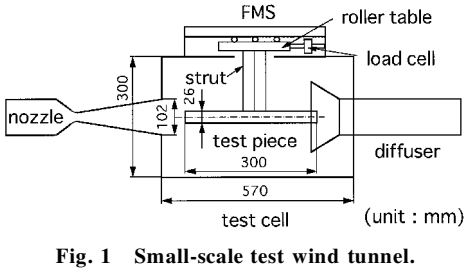

Fig. 1 Small-scale test wind tunnel.

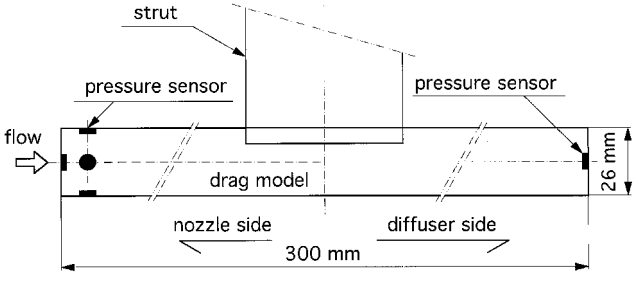

Fig. 2 Parallelepiped drag model.

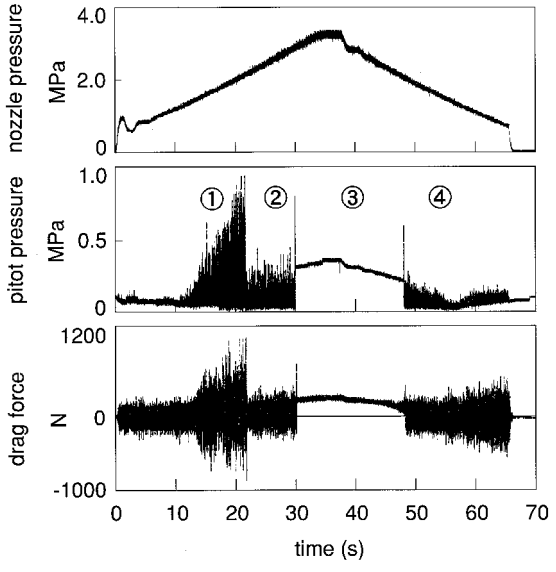

Fig. 3 Variations of pitot pressure and drag.

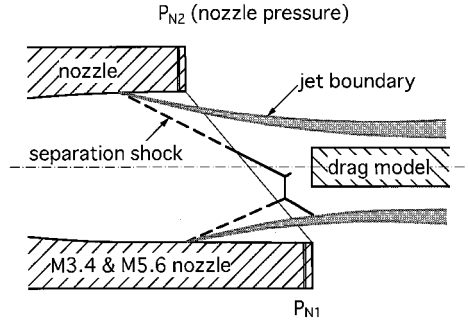

Fig. 4 Flowfield during wind-tunnel starting.

sure on the model was much shorter than the duration with low pressure. During low pressure, the ratio of the front pressure to the test cell pressure was less than the sonic pressure ratio for air (1.89). This implies that the model was immersed in subsonic flow for a considerable duration of time and was impinged on intermittently by supersonic flow slower than the design Mach number, which means less total pressure loss.

Because the nozzle flow overexpands before the wind-tunnel start and separates in the middle of the nozzle, it is recompressed with oblique shock waves. Such oblique shock waves were often observed in the experiments. Pitot pressure of the flow decelerated by an oblique shock wave rises to a point several times higher than that of the flow decelerated with a single normal shock. In such a way, the high pitot pressure observed in region ① is explained as being caused by intermittent impingement on the model by the low Mach number supersonic flow generated by separation in the middle of the nozzle.

These pitot pressures were about three times higher than the pitot pressures expected by the design Mach numbers. Higher pitot pressure is possible if the separation point moves upstream in the nozzle. However, these high pressures only intermittently and randomly acted on the model front. Therefore, statistical analysis using fast Fourier transform (FFT) was the next subject to be investigated.

Spectra of Force and Pressure

Averaged spectra density of load cell force and force calculated from pitot pressure in region ① are shown in Fig. 5; the relation between the load cell output and the front pressure that is the input of load fluctuation was investigated. Figure 5a shows the power spectral density of F_p. Pressure drag, which is the input of the FMS, was dominant in the frequency region lower than 200 Hz. On the other hand, the power spectrum of the load cell had peaks around 160, 510, and 660 Hz, as shown in Fig. 5b. These frequencies of vibration modes were identified by impulse hammering tests. The 160-Hz peak showed the resonance of the pitching mode of the model and the strut, and the 510-Hz peak showed the axial resonance mode of the FMS.

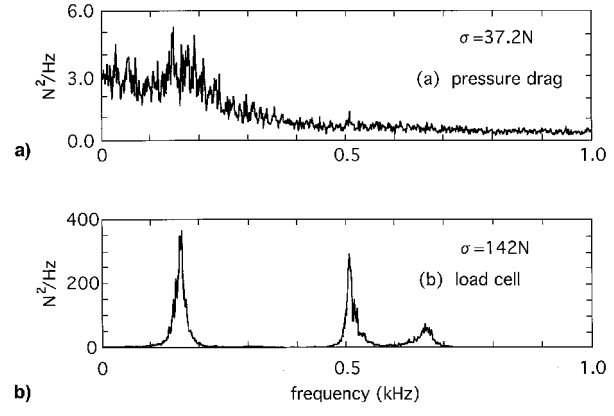

Fig. 5 Power spectral density of a) pressure drag and b) load cell output.

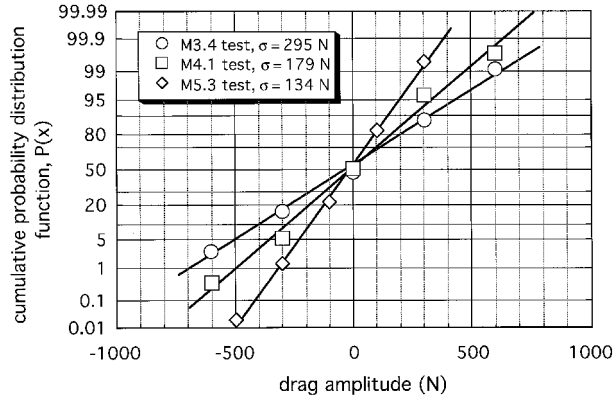

Fig. 6 Probability distribution of drag amplitude.

The standard deviation of $X(t)$, $\boldsymbol{\sigma}$, is shown in Figs. 5a and 5b, at the upper right of each figure. The σ is given as an integral of power spectral density, in the frequency domain. The σ of pressure drag was 37.2 N and that of load cell was 142 N. These results mean that the standard deviation of the FMS load was amplified by resonance of the FMS to a level 3.8 times the input value of pressure drag.

Expected Value of Maximum Peak Amplitude

To discuss maximum peak amplitude, the FMS output signal was analyzed in the amplitude domain in addition to the analyses in the time and frequency domains. Figure 6 shows the cumulative probability distribution function of drag amplitude $P(x)$. The vertical axis is shown in a normal probability distribution scale in which the normal probability distribution is expressed by linear lines. As shown in Fig. 6, the cumulative probability distribution functions of drag amplitude for three Mach number experiments are linear. Therefore, a normal probability distribution was assumed for the drag amplitude distribution. If the normal (Gaussian) probability distribution with σ is assumed, the expected maximum peak factor is expressed as a function of σ and the number of peaks.[12] The expected maximum peak factor increases with the increase of the total number of peaks. Therefore, higher natural frequency of the system and longer test duration increase the expected maximum peak factor.

Test results in the small-scale wind tunnel showed that the σ in the amplitude of unsteady frontal pressure can be correlated with the dynamic pressure. This suggests that the unsteady load can be correlated with drag coefficient. Test results of maximum peak loads correlated with drag coefficient will be discussed in the last section.

Test of Engine Models

Ramjet Engine Test Model and Test Procedures

To evaluate the dynamic loads caused by engine unstart, tests were carried out to simulate engine unstart conditions by secondary gas injection into a one-fourth-scale model of the CH4-fueled subscale ramjet engine for the hypersonic civil transport (HYPR). This model is designated 1/4-HYPR, and the subscale ramjet engine is designated 1/1-HYPR hereafter. Figure 7 shows the 1/4-HYPR model, the design Mach number of which is 5.5. The configuration of the external and the internal portions of the diffuser is exactly scaled down in the model. Secondary flow gas (N_2) is injected into the model through the line designated GN_2 in Fig. 7 to shift the mass flow rate conditions. The maximum flow rate of the secondary flow gas is about 20% of the main flow rate. The model was tested in the small-scale wind tunnel.

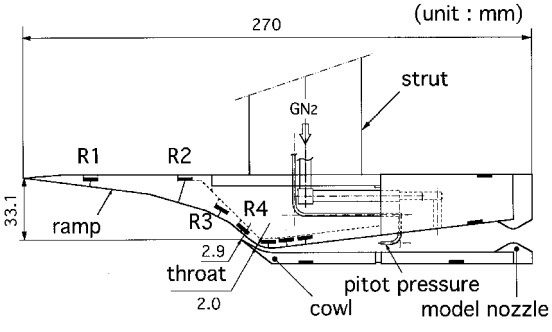

Fig. 7 Ramjet engine test model (1/4-HYPR).

The model is equipped with a two-dimensional, four-staged intake with a width of 25 mm and a height of 33.1 mm. The angles of the ramps were designed so that the shock waves are focused close to the cowl lip at the design Mach number of 5.5. The design total compression ratio including internal compression is 300. To obtain the best performance, the oblique shocks generated by the four-staged ramp were chosen to be of equal strength. The turning angles of ramp 1–4 are 7.5, 8.9, 10.5, and 12.7 deg, respectively. Under the on-design conditions, the flow decelerates to Mach 2.5 at the fourth ramp and enters the isentropic turning region (the internal diffuser). Deceleration to a subsonic speed is achieved by a normal shock behind the throat with a height of 2 mm.

The contraction ratio in the internal diffuser (1.45) of this fixed geometry model without any bleeding is slightly larger than the critical value (1.32) estimated by the Kantrowitz–Donaldson criteria. Therefore, the internal diffuser may fail to swallow shock for inlet starting. However, the capture ratio in this model was found to be 0.65, which is close to the capture ratio measured in the 1/1-HYPR[13–14] inlet. In the 1/1-HYPR, there is a bleed system in the fourth ramp and one in the throat of the internal diffuser. We confirmed start of the 1/1-HYPR inlet by the shock patterns in the inlet by the schlieren method and by the independence of the capture ratio from the back pressure (the supercritical operation).

Therefore, it was concluded that the inlet of the 1/4-HYPR operated in high subcritical flow conditions, where detached shock and spilling are found at the cowl. Increasing back pressure pushes the shock system upstream and leads the inlet into buzzing. In the present study, observation of unstable oscillation of engines was the main purpose. The high subcritical operation of the 1/4-HYPR inlet did not deteriorate the inlet performance so severely. Therefore, the onset of buzz is defined as the unstarting of engine in this paper.

The exit nozzle area was chosen to initially prevent the buzz. Then secondary flow gas (N_2) was injected into the model to put it into the buzz zone. Thus, engine unstart condition was simulated by the addition of mass instead of the addition of heat to engines.

Flowfield of Unstarting Ramjet Engine

Figure 8 shows pressure variation of the 1/4-HYPR model during a Mach 4.1 test in logarithmic scale. Pressure is nondimensionalized by P_0. At 19 s, the wind tunnel started. The wall pressure of the first ramp (ramp 1) changed considerably in the steady-state operation stage. Drifting of the pressure sensor because of temperature change or some malfunction of the sensor occurred. This change was about 8% of the full scale of the sensor. It might not be reasonable to discuss precise steady pressure with wideband pressure data, especially in the low-pressure region, because a large maximum-pressure sensor has to be used to withstand peak oscillating pressure higher than steady pressure.

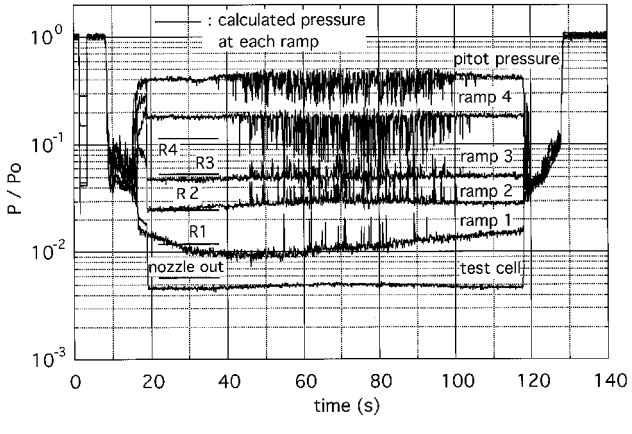

Fig. 8 Pressure variation during 1/4-HYPR model unstart.

The compression ratio of each ramp, 1–4, before the unstable oscillation, was 2.3, 2.4, 1.9, and 3.7, respectively, under Mach 4.1 test conditions. With four ramps, a compression ratio of 39 was obtained. The calculated compression ratio for one-dimensional inviscid flow of each ramp is 2.1, and a compression ratio of 19 was obtained with four ramps. The large discrepancy of the fourth-ramp value possibly was caused by high subcritical operation. The pressure recovery factor of pitot pressure in the diffuser was 0.4. The pitot pressure rose to 0.45 from 35 s because of secondary flow injection. From around 40 s, unstable operation gradually began and the pressure of ramp 4 in the downstream region began to fluctuate in the direction of low pressure. With the increase of secondary flow rate, this effect reached ramps 3 and 2 in the upstream region. With a further increase of secondary flow injection, the pressure of ramps 1–3 in the upstream region began to fluctuate in the direction of high pressure. After 47 s, the effect of unstart reached ramp 1. In this experiment, as the pressure of secondary flow injection was reduced gradually from 90 s, the engine stabilized again from around 105 s.

The flowfield of the unstart engine may be explained as follows. With the increase of secondary flow injection pressure, the detached shock wave moves upstream. When the operating condition goes into the region where a further decrease of main flow reduces pressure recovery factor, the compression system becomes unstable. The separation spreads along the ramp intermittently in this condition, and goes upstream as a separation bubble. Synchronized with this phenomenon, the pressure of ramp 4 decreases and the pressure of ramp 3 increases. When the strength of unstart becomes stronger, the separation bubble travels further upstream and the pressure of ramps 2 and 1 also begin to fluctuate in the direction of high pressure caused by the compression by separation shock.

Injection of secondary flow into the model continuously changed the frequency of the pressure oscillation caused by engine unstart, in the range lower than 190 Hz. Just before engine oscillation began, an intermittent slight pressure spike was observed on the walls. With the increase of secondary flow injection pressure, the frequency of the pressure spike increased. At least in this experiment, engine oscillation did not begin suddenly without the aforementioned slight pressure spike. Therefore, engine unstart was easily predicted by monitoring instantaneous pressure around the inlet throat. The strength of engine unstart depended on spike frequency.

The inside flow of the model was subsonic and the inside pressure was homogeneous. Therefore, pressure drag inside the model was small. Most of the pressure drag was generated by the region around ramp 4 where the pressure was high. The pressure spike of ramp 4, which fluctuated in the direction of low pressure during the engine unstart in Fig. 8, caused pressure drag reduction. Precise observation of the drag and the ramp 4 pressure showed that FMS load began to move toward the direction of thrust and that the ramp 4 pressure began to decrease at the moment when engine oscillation began.

Test Scramjet Engine

Figure 9 shows the scramjet engine tested. Its overall length was 2100 mm. The width of the entrance was 200 mm. The height of the entrance was 250 mm. The exit width and height were the same as those of the entrance. The engine was composed of four components: 1) inlet, 2) isolator, 3) combustor, and 4) nozzle. The inlet was a sidewall compression type with a 6-deg half-wedge angle, and a contraction ratio of 3. The leading edge of the inlet was swept back 45 deg to deflect the airstream for suitable spillage required for starting at low Mach numbers. Hydrogen fuel was injected by four injectors: 1) main parallel, 2) main vertical, 3) pilot sidewall, and 4) pilot top wall. Two plasma torch ignitors of 2.5 kW were used for ignition at the top wall. A wideband pressure sensor was installed on the sidewall at a position 100 mm apart from the top wall and 100 mm upstream of the isolator inlet.

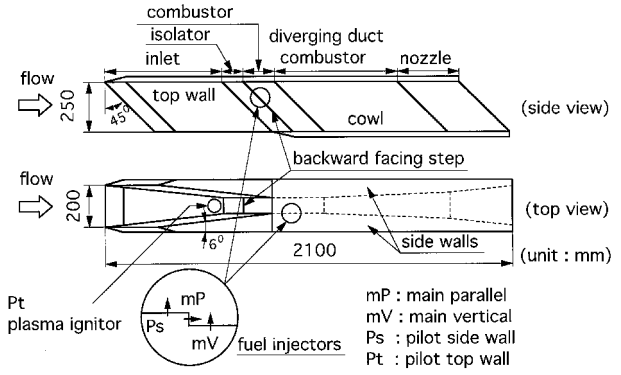

Fig. 9 Scramjet test engine.

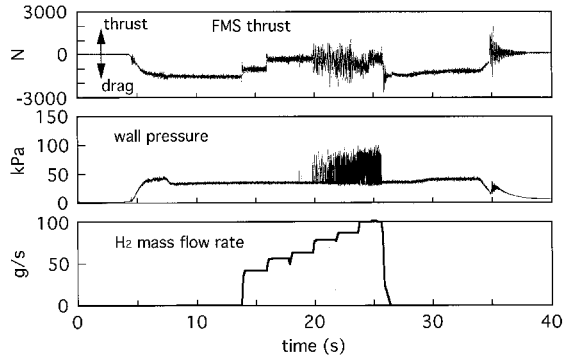

Fig. 10 Thrust and wall pressure of the scramjet engine under Mach 4 flight conditions.

The scramjet engine was installed on an FMS and tested in the large-scale wind-tunnel, RJTF. The size of the nozzle exit of RJTF was 510 mm × 510 mm. The blockage ratio of the engine including sidewall fairing and cowl thickness was about 25%. The test cell, 5.1 m in length and 3 m in diameter, was evacuated by a steam ejector system. Details of the RJTF are shown in Ref. 3.

Scramjet Engine Testing

In Fig. 10, histories of thrust and wall pressure measured in the engine test of Mach 4 flight conditions are illustrated with the main H_2 flow rate. Flight Mach number 4 ($M4$) corresponds to the engine inlet Mach number 3.4. Details of $M4$ tests are shown in Ref. 11. Because the RJTF flow is exhausted by a two-stage steam-ejector system, the wind tunnel started just after pressurization of the RJTF nozzle began (4.3 s in Fig. 10). As a result, the load at the wind-tunnel start was small. An $M4$ flow of 900 K was established at 8 s, and the engine test was conducted from 14 to 26 s. The large oscillation of drag found at 35 s was caused by the break of the $M4$ flow in the wind tunnel. Thus, the load imposed on the FMS during the starting process of the wind tunnel was much smaller than that of the flow break during the stopping process and that of the engine unstart mentioned later in this paper.

An engine drag of 1580 N was measured between 8 and 14 s. The H_2 total mass flow rate in Fig. 10 shows the main vertical injection flow rate plus pilot flow rate 12 g/s. A total flow rate of 42 g/s was supplied from 14 s, and the H_2 flow rate was increased up to 100 g/s step by step. The maximum fuel flow rate corresponded to the bulk equivalence ratio of 0.7 for the airflow captured by the engine inlet.

With increasing H_2 flow rate, the engine drag decreased to 370 N at an H_2 flow rate of 56 g/s (16 s), which means that a gross thrust of 1210 N was delivered by the engine combustion. However, the engine suffered an unstart condition when the fuel flow rate was increased up to 78 g/s (20 s). Here, unstart is defined as a condition in which a strong unsteady interaction between the inlet and combustor exists. The thrust measured with the FMS and the wall pressure measured at the sidewall of the inlet began to oscillate violently in this condition. The peak pressure became more than two times greater than the value under the engine start conditions, and the peak amplitude of the thrust became comparable to the value of the engine drag.

Although it is not clear from Fig. 10, the frequency of the pressure spikes increased with the strength of unstart. The FFT analysis of the pressure pulse data indicated broad power spectral density distributions in the unstart conditions of the scramjet engine, unlike those in the ramjet engine. The power spectral density distribution shifted to a higher frequency region with the increase of fuel flow rate. The decrease in amplitude of load cell output, in spite of large oscillation of wall pressure at 24 s, can be attributed to separation of the pulse frequency from the resonance frequency of the FMS.

Engine unstart can be detected with pressure sensors flash-mounted on the engine wall. For instance, isolated pressure spikes observed at 19 s in Fig. 10 indicated that the engine was approaching unstart conditions. The spikes were sparse at the beginning, and became frequent in severe unstart conditions. Hence, engine unstart can be prevented and controlled by monitoring the wall pressure with wideband sensors and by adjusting the fuel flow rate before the engine thrust oscillation resonate with FMS.

The wideband wall pressure was monitored at both sides of the inlet. The time lag between the pressure spikes measured at the two axisymmetrically located positions was investigated under engine unstart conditions. There was no time lag between the two signals. This suggests that a large separation bubble developed and fluctuated in the streamwise direction in the unstart conditions.

Maximum Peak Loads

As mentioned earlier, test results in the small-scale wind tunnel suggested that an unsteady load can be correlated with drag coefficient. Figure 11 illustrates the relation between C_{dp} and the steady C_d of the models. The C_d of models was 0.2–0.4 for the scramjet engine tested in RJTF, 0.7 for the 1/4-HYPR ramjet model in the small-scale wind tunnel, and 1.8 for the rectangular parallelepiped drag model in the small-scale wind tunnel. These drag coefficients include the contribution of the supporting strut and the fairing for the engine.

Each symbol in Fig. 11 denotes the mean value of some experiments. Error bars in Fig. 11 indicate data uncertainty. Peak loads were measured by the FMS under unlocked conditions. All of the peak load coefficients for the large-scale wind tunnel (RJTF) and the small-scale tunnel roughly fit a straight line with $C_{dp} = 5C_d$. Figure 11 indicates that the peak load coefficients are roughly proportional to the drag coefficients, although scale effects exist. The C_{dp}/C_d value of the small-scale model tended to be larger. The difference of natural frequencies among the FMSs including models is considered to be the source of the scale effect.

The reason the starting load of the scramjet engine tested in RJTF is small can be explained as follows. The nozzle total pressure to start the RJTF is 0.12 MPa in the $M4$ test condition and 1.2 MPa in the $M6$ condition. These pressures are much lower than the test pressure of 0.9 MPa ($M4$) and 4.6 MPa ($M6$), respectively. Flight Mach numbers 4 ($M4$) and 6 ($M6$) correspond to the engine inlet Mach numbers 3.4 and 5.3, respectively. The air evacuation system in the RJTF, driven by the two-stage steam ejector, is very powerful and the RJTF can easily start with these lower nozzle total pressure. Hence, the dynamic pressure to start the wind tunnel is lower in the RJTF. In addition, the drag coefficient of the scramjet engine was much smaller than that of the drag model of rectangular parallelepiped. Thus, the negligible starting loads in the scramjet engine testing can be attributed to the lower dynamic pressure and the low drag coefficients of the engine.

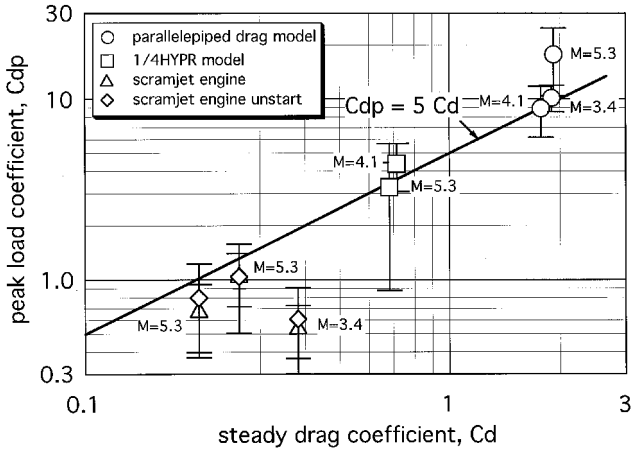

Fig. 11 Correlation between steady drag coefficient and peak load coefficient.

The amplification factor of n ($=C_{dp}/C_d$) between the peak load coefficient and the drag coefficient is interpreted as follows. Random loads imposed on the model are transmitted to load cells and amplified in the FMS. The dynamic response of the small-scale FMS was measured and the amplitude gain of FMS was determined by dividing the σ of the input and the σ of the output. For instance, the small-scale FMS amplifies the σ of the input load by 3.8 as shown in Fig. 5. The expected maximum peak factor over the σ can also be calculated in any random data if the Gaussian probability distribution is confirmed as in the case of Fig. 6. Our estimation shows that peak loads nearly three times greater than the variance may be observed in the FMS during the test span. The factor of n could be explained as the product of the amplitude gain of FMS and the expected maximum peak factor for random phenomena.

Peak load coefficients of the scramjet engine unstart loads are also plotted in Fig. 11 along with the peak load coefficients of the wind-tunnel starting loads. The values of C_{dp} of the scramjet engine unstart conditions ($\diamond$) were nearly the same as those of the starting loads of the wind tunnels ($\triangle$). For example, C_d of the scramjet engine with a full-height strut for the $M5.3$ condition ($M6$ flight condition) was 0.26 and C_{dp} of this condition was 1.05 ± 0.55. C_d of the scramjet engine with a one-fifth-height strut for the $M5.3$ condition was 0.21, and C_{dp} of this condition was 0.80 ± 0.43. Thus, peak load coefficients of both the scramjet engine unstart and the starting load of the wind tunnel were about five times larger than that of the steady drag.

Although the maximum peak load coefficient of the starting load is several times larger than steady drag coefficient, it can be reduced by decreasing the starting nozzle pressure with a powerful exhaust system. However, in the case of engine unstart load, it is impossible to reduce the load by decreasing nozzle operating pressure. Therefore, the engine unstart load is a more serious problem than the starting load of wind tunnels. The engine unstart loads must be expected to be five times larger than the steady loads if the engine unstart loads are to be measured under FMS unlock conditions.

Conclusions

Starting loads of hypersonic wind tunnels and unsteady loads because of engine unstart conditions were measured by unlocked FMSs. The following conclusions were drawn from the test results.

1) The magnitude of the starting loads and engine unstart loads was correlated to the drag coefficient of the models. The maximum peak load coefficients were several times greater than the drag coefficients. The magnification factor was explained as being the product of the FMS gain and the expected maximum peak factor, and affected by the natural frequency of the FMSs.

2) Formation of a separation bubble that travels up the inlet region can be postulated for explanation of the unstable oscillation of the engine. Before strong engine unstart begins, pressure spikes appear around the inlet area intermittently, and the frequency of this spike increases with the strength of engine unstart. Consequently, severe engine unstart can be predicted by monitoring wideband pressure.

3) Both ramjet and scramjet engines showed unstable oscillating conditions at some fuel flow rates, which caused pressure and thrust fluctuations. The oscillation frequency was apparent in the ramjet engine; it was, therefore, possible to avoid resonance with the FMS. However, the oscillation was random in the scramjet engine and therefore it was difficult to avoid resonance.

References

[1]Pope, A., and Goin, K. L., *High-Speed Wind Tunnel Testing*, Krieger, New York, 1978, p. 365.

[2]Maydew, R. C., "Compilation and Correlation of Model Starting Loads from Several Supersonic Wind Tunnels," Sandia Rept., SC-4691 (RR), June 1962.

[3]Miyajima, H., "Scramjet Research at the National Aerospace Laboratory," AIAA Paper 91-5076, Dec. 1991.

[4]Trimpi, R. L., "A Theory for Stability and Buzz Pulsation Amplitude in Ram Jets and an Experimental Investigation Including Scale Effects," NACA Rept. 1265, 1956.

[5]Seddon, J., and Goldsmith, E. L., *Intake Aerodynamics*, William Collins Sons & Co. Ltd., London, 1985, pp. 269–291.

[6]Rodi, P. E., Emami, S., and Trexler, C. A., "Unsteady Pressure Behavior in a Ramjet/Scramjet Inlet," *Journal of Propulsion and Power*, Vol. 12, No. 3, 1996, pp. 486–493.

[7]Ichimaru, O., Ishizuka, M., and Murashima, K., "Overview of the Japanese National Project for Super/Hypersonic Transport Propulsion System," American Society of Mechanical Engineers, 92-GT-252, June 1992.

[8]Yatsuyanagi, N., Chinzei, N., and Miki, Y., "Initial Tests of a Sub-Scale Scramjet Engine," *12th ISABE* (Melbourne, Australia), Vol. 2, AIAA, Washington, DC, 1995, pp. 1330–1335.

[9]Kanda, T., Hiraiwa, T., Mitani, T., Tomioka, S., and Chinzei, N., "Mach 6 Testing of a Scramjet Engine Model," *Journal of Propulsion and Power*, Vol. 13, No. 4, 1997, pp. 543–551.

[10]Saito, T., Wakamatsu, Y., Mitani, T., Chinzei, N., and Shimura, T., "Mach 8 Testing of a Scramjet Engine Model," 20th International Symposium on Space Technology and Science (Gifu, Japan), Paper 96-a-2-11, May 1996.

[11]Sunami, T., Sakuranaka, N., Tani, K., Hiraiwa, T., and Shimura, T., "Mach 4 Tests of a Scramjet Engine—Effects of Isolator," *13th ISABE*, Vol. 1, AIAA, Reston, VA, 1997, pp. 615–625.

[12]Harris, C., and Crede C., *Shock and Vibration Handbook*, McGraw–Hill, New York, 1976.

[13]Enomoto, Y., Fujimoto, A., Kimura, H., Fujiwara, K., Mitani, T., and Yanagi, R., "Experimental Study of Mach 5 Fixed Geometry Inlet for Subscale Ramjet Engine Test," *13th ISABE*, Vol. 1, AIAA, Reston, VA, 1997, pp. 212–219.

[14]Futamura, H., Enomoto, Y., Ohshima, T., Kimura, H., Fujiwara, K., Kinoshita, Y., Nakahishi, H., Kishi, K., Mitani, T., and Yanagi, R., "Freejet Test of Ramjet System for Hypersonic Transport Vehicle," *13th ISABE*, Vol. 1, AIAA, Reston, VA, 1997, pp. 573–581.